

See discussions, stats, and author profiles for this publication at: <https://www.researchgate.net/publication/231647501>

# Intrinsic Kinetics of Gypsum and Calcium Sulfate Anhydrite Dissolution: Surface Selective Studies under Hydrodynamic Control and the Effect of Additives

ARTICLE *in* THE JOURNAL OF PHYSICAL CHEMISTRY C · MAY 2011

Impact Factor: 4.77 · DOI: 10.1021/jp201718b

---

CITATIONS

15

---

READS

16

5 AUTHORS, INCLUDING:



[Martin Andrew Edwards](#)

University of Utah

37 PUBLICATIONS 519 CITATIONS

SEE PROFILE



[Massimo Peruffo](#)

Johnson Matthey

17 PUBLICATIONS 105 CITATIONS

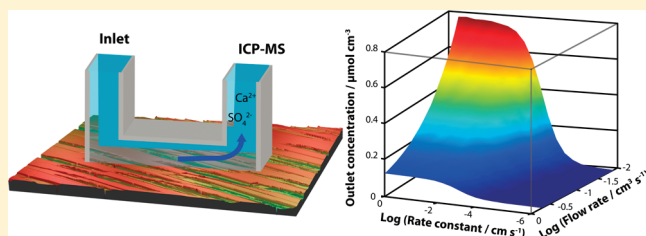
SEE PROFILE

# Intrinsic Kinetics of Gypsum and Calcium Sulfate Anhydrite Dissolution: Surface Selective Studies under Hydrodynamic Control and the Effect of Additives

Michael M. Mbogoro, Michael E. Snowden, Martin A. Edwards, Massimo Peruffo, and Patrick R. Unwin\*

Department of Chemistry, University of Warwick, Coventry, CV4 7AL, United Kingdom

**ABSTRACT:** The intrinsic dissolution activity of the basal (010) and edge (001) surfaces of gypsum and polycrystalline calcium sulfate anhydrite crystals has been investigated, under far from equilibrium conditions, via the channel flow cell (CFC) method with off-line inductively coupled plasma-mass spectrometry (ICP-MS) for the measurement of dissolved  $\text{Ca}^{2+}$  from the crystal surface. This approach allows measurements to be made over a wide range of flow rates so that the importance of mass transport versus surface kinetics can be elucidated. Complementary quantitative modeling of the dissolution process was carried out by formulating convective–diffusive equations that describe mass transport in the CFC, coupled to a boundary condition for dissolution of the crystal surface. We found that a linear rate law applied, and intrinsic dissolution fluxes were deduced. The following dissolution fluxes,  $J_0 = k_{\text{diss}} \times c_{\text{eq}}$  were measured, where  $k_{\text{diss}}$  is the dissolution rate constant and  $c_{\text{eq}}$  the calcium sulfate concentration in saturated solution:  $5.7 (\pm 1.4) \times 10^{-9} \text{ mol cm}^{-2} \text{ s}^{-1}$  for basal plane gypsum and  $4.1 (\pm 0.7) \times 10^{-9} \text{ mol cm}^{-2} \text{ s}^{-1}$  for calcium sulfate anhydrite. Edge plane gypsum, under the experimental conditions applied, was found to dissolve at a mass transport-controlled rate. The effects of *l*-tartaric acid, *d*-tartaric acid, and sodium trimetaphosphate (STMP) as important potential additives of the dissolution process of basal plane gypsum were investigated. It was found that the tartaric acids had little effect but that STMP significantly retarded gypsum dissolution with  $J_0 = 1.6 (\pm 0.6) \times 10^{-9} \text{ mol cm}^{-2} \text{ s}^{-1}$  (5 mM STMP solution). The mode of action of STMP was further elucidated via etch pit morphology studies.



## 1. INTRODUCTION

Among the rock-forming minerals, gypsum ( $\text{CaSO}_4 \cdot 2\text{H}_2\text{O}$ ) and related calcium sulfate materials, such as the hemihydrate ( $\text{CaSO}_4 \cdot 0.5\text{H}_2\text{O}$ ) and anhydrite ( $\text{CaSO}_4$ ), are abundant in nature, with extensive deposits underlying an estimated 25% of the global surface.<sup>1</sup>  $\text{CaSO}_4$  minerals play an important role in the evolution of karst systems<sup>2</sup> and in numerous geochemical phenomena;<sup>3,4</sup> they are also utilized extensively in metallurgical processes<sup>5</sup> and in construction and manufacturing.<sup>6,7</sup> Furthermore, the formation of these minerals causes significant scaling problems, particularly in petroleum technology.<sup>8,9</sup> Studies of dissolution/growth kinetics and mechanisms are pertinent to all these areas in order to develop the knowledge and understanding of natural systems and to optimize the use of  $\text{CaSO}_4$  minerals in technological applications.<sup>10,11</sup>

The dissolution of gypsum has been studied by many techniques, ranging from macroscopic kinetic measurements on particulate systems<sup>12</sup> to high-resolution microscopic studies using atomic force microscopy (AFM).<sup>13</sup> A recent review by Colombani<sup>14</sup> sought to correlate various macroscopic kinetic measurements of gypsum dissolution in order to extract a unified surface dissolution rate, by estimating the likely mass transport rates associated with different techniques. An intrinsic *surface dissolution rate constant* into free solution (maximum undersaturation at the crystal/solution interface) was deduced to be  $J_0 = 5 \pm 2 \times 10^{-9} \text{ mol cm}^{-2} \text{ s}^{-1}$ , as the intercept of a reciprocal rate – reciprocal

mass transport plot. Some confidence in this assignment comes from the fact that the techniques surveyed included the rotating disk (RD) method, which delivers well-defined mass transport. However, in many cases, the techniques used previously have been characterized by poorly defined and/or low mass transport conditions, making it difficult to assign surface kinetics from individual studies. Furthermore, many previous investigations have employed polycrystalline material so that different crystal faces, edges, and corners are exposed to solution, which are likely to have different dissolution characteristics. To further improve our understanding of dissolution kinetics, surface-selective studies under well-defined mass transport conditions are imperative. Such studies are the focus of this paper.

Calcium sulfate anhydrite dissolution has also been investigated, but not as extensively as gypsum. Because the solubility of gypsum is less than that of anhydrite,<sup>15</sup> reliable anhydrite dissolution data may only be obtained under far from equilibrium conditions where the concentration of dissolved products near the crystal surface is below the saturation level with respect to gypsum.<sup>16</sup> Higher surface concentration may lead to precipitation of gypsum on the surface of the dissolving anhydrite crystal, thereby forming a protective layer that inhibits further dissolution.<sup>2,16</sup>

**Received:** February 21, 2011

**Revised:** April 19, 2011

**Published:** May 03, 2011

An early rotating disk (RD) study on polycrystalline anhydrite found a rather high intrinsic dissolution flux of  $J_0 = 2 \pm 1 \times 10^{-8} \text{ mol cm}^{-2} \text{ s}^{-1}$ .<sup>12b</sup> However, subsequent free drift batch investigations on particulates<sup>16</sup> deduced much lower rates,  $J_0 = 5 \pm 1 \times 10^{-9} \text{ mol cm}^{-2} \text{ s}^{-1}$ , which have been corroborated by other studies.<sup>1</sup>

A further important aspect of crystal dissolution is the role of additives. This is of particular relevance for  $\text{CaSO}_4$  minerals (notably gypsum) used in construction, where additives are used to passivate dissolution, so as to retard physicochemical deterioration by processes, such as humid creep, caused by environmental factors, such as rainwater and atmospheric pollutants.<sup>17</sup> However, in contrast to calcium carbonate minerals, for example, where the role of additives has been explored extensively,<sup>18,19</sup> relatively few gypsum dissolution studies have considered the influence of additives. Such studies would be valuable to elucidate the effect of additives on the durability and versatility of  $\text{CaSO}_4$ -based materials,<sup>20,21</sup> and so, a further aspect of this paper is to examine the mode of action of key additives on gypsum dissolution.

As highlighted herein, to understand mineral/liquid reaction kinetics, experimental techniques need to be able to quantitatively separate mass transport and surface kinetic effects<sup>22,23</sup> and ideally allow the study of well-defined surfaces. To this end, the channel flow cell (CFC) method has proven particularly powerful for studying dissolution processes.<sup>24,25</sup> This technique typically involves locating the crystal substrate of interest flush in the base wall of a rectangular duct through which solution flows under laminar conditions. Well-defined flow allows accurate modeling of mass transport within the flow cell chamber. Furthermore, because mass transport rates are controllable over a wide range, their influence on dissolution rates can be elucidated quantitatively.<sup>24–26</sup> The CFC method permits rate laws governing a dissolution reaction to be proposed and tested by comparing experimental data to the predictions from mass transport–chemical reactivity models.<sup>24,25</sup> Hitherto, dissolution in the CFC method has typically been monitored by the use of local electrochemical measurements<sup>24–27</sup> to provide in situ detection of the dissolution process. However, some types of electrodes, for example,  $\text{Ca}^{2+}$  ion selective electrodes, are rather fragile and difficult to deploy in such cells.<sup>28</sup> We address this issue herein using a different approach for  $\text{Ca}^{2+}$  analysis.

Most CFC designs comprise two-part or three-part assemblies typically held together with nuts and bolts, to produce channels, typically 40 mm in length, 6–10 mm across, and 0.2–1 mm high.<sup>27</sup> Such cells place some restrictions on sample size and the way in which crystal materials are presented for study. We have recently introduced a new CFC design and fabrication procedure using microstereo lithography (MSL) to produce radically miniaturized one-part CFC units.<sup>29</sup> CFC units fashioned in this way eliminate awkward assembly (nuts, bolts, or adhesive sealants) and greatly reduce the cell volume, without compromising mass transport. Indeed, a much wider range of mass transport rates can be implemented. The MSL-CFC is assembled by simply placing a CFC unit on the substrate of interest and securing with light pressure or even a thread!

Herein, we couple the CFC technique with off-line inductively coupled-mass spectrometry (ICP-MS) for the measurement of dissolved  $\text{Ca}^{2+}$  from the crystal surface, collected from the CFC effluent, over a wide range of flow rates. This is effective because of the miniaturized flow cell unit and short wash-out time of the cell (vide infra). For the purposes of quantitative modeling, we formulate convective–diffusive equations for mass transport in

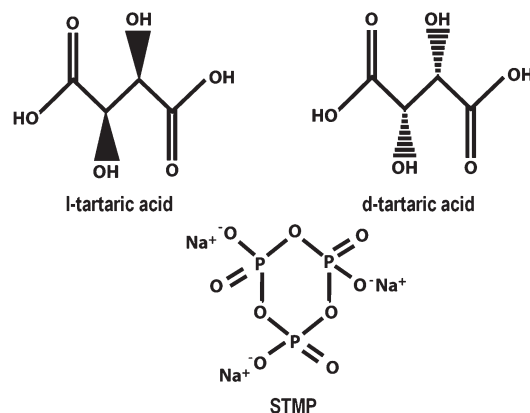


**Figure 1.** Molecular structures of the additives used for some of the dissolution studies.

the CFC, coupled to a boundary condition for the crystal surface, which describes the dissolution process. In this way, we are able to predict the outlet  $\text{Ca}^{2+}$  concentration for analysis of experimental data. Using this approach, we provide intrinsic rates for the dissolution of the basal cleavage (010) and edge (001) plane surfaces of gypsum, in order to elucidate any differences in magnitude for the first time. Furthermore, we elucidate the effect of key additives on dissolution from basal plane gypsum, in order to identify any kinetic influences and morphological effects. Finally, we investigate the dissolution of polycrystalline anhydrite, to resolve the discrepancy in kinetics highlighted above and to further demonstrate the capability of the methodology.

## 2. EXPERIMENTAL SECTION

**2.1. Samples.** Natural gypsum single-crystal samples (St. Gobain Gyproc) were prepared by breaking large selenite crystals into manageable pieces ( $\sim 5 \text{ cm}^2$ ) and cleaving along the (010) plane with a sharp razor blade. Careful cleavage on this plane produced clean, fresh surfaces largely devoid of macrosteps. Polycrystalline anhydrite (UKGE Limited) and (001) edge plane gypsum samples (exposed surface  $\sim 8 \text{ cm}^2$ ) were embedded in epoxy resin molds (Delta Resins Ltd.). These samples (anhydrite and edge plane gypsum) were first polished with silicon carbide 4000 grit paper (Buehler) and further on a pad with  $6 \mu\text{m}$  diamond spray (Kemet Int Ltd.), followed by thorough rinsing in ultrapure  $\text{H}_2\text{O}$ . For each experiment, a fresh surface was fashioned by polishing the surface of the embedded crystal. Surfaces were etched before studies (vide infra) to ensure a contaminant-free surface.

**2.2. Solutions.** All solutions were prepared using ultrapure water (Milli-Q Reagent, Millipore) with a typical resistivity of  $18.2 \text{ M}\Omega \text{ cm}$  at  $25^\circ\text{C}$ . Most experiments were run in ultrapure water, but some measurements were made in 5 mM solutions of the additives of interest (Figure 1); these were sodium trimetaphosphate (STMP), d-tartaric acid, and l-tartaric acid (all from Sigma). In addition, a solution of 0.03 M  $\text{KNO}_3$  (Sigma) was used as an ionic strength match in some experiments for comparison to the 5 mM STMP solution. Ionic strength and chemical speciation were calculated using the numerical code MINEQL+ (Environmental Research Software, version 4.5).<sup>30</sup> Table 1 summarizes all additive solutions used, with the input concentrations, and resulting pH and ionic strength values. The Davies equation was used to calculate the activity coefficients for

**Table 1.** Additives Used for CFC Dissolution Studies on Basal Plane Gypsum Crystal

additive	concentration (mM)	pH	ionic strength (mM)
<i>l</i> -tartaric acid	5	2.71	19
<i>d</i> -tartaric acid	5	2.70	19
STMP	5	5.88	30

each solution.<sup>31</sup> The solubility products ( $K_{sp}$ ) of gypsum and anhydrite were  $3.14 \times 10^{-5}$  and  $4.93 \times 10^{-5}$ , respectively.<sup>15</sup>

**2.3. Sample Preparation and Surface Roughness Determination.** An important consideration in dissolution studies is the initial surface morphology or roughness and how this changes during the course of the reaction. Several studies have attempted to establish a consensus on an appropriate way to normalize dissolution rates for studies where the surface area changes.<sup>32</sup> We addressed this issue by initially etching samples with the expectation (validated, vide infra) that they would maintain a constant specific surface area during the course of dissolution. Thus, prior to CFC experiments, each sample was etched in a large volume ( $>500 \text{ cm}^3$ ) of ultrapure  $\text{H}_2\text{O}$  at  $22 \pm 1^\circ\text{C}$  in a beaker stirred with a magnetic flea. After  $\sim 30$  min, the sample was withdrawn and immediately dried with a strong burst of  $\text{N}_2$  gas (BOC). By etching the surface before CFC studies, we produced surfaces with a roughness factor,  $\lambda$  (specific surface area/geometric area), mostly close to unity, but occasionally several times larger, depending on the sample (vide infra). An early study by Bruckenstein<sup>33</sup> found that mass transport to a rotating disk electrode (RDE) for a large dynamic range of rotation speeds was unaffected by  $\lambda$  values up to 7.5. Because the RDE and the CFC have similar mass transport rates,<sup>26,34</sup> it was reasonable to assume that the sample preparation procedure used would not significantly perturb mass transport in the CFC. To determine  $\lambda$  for the different etched substrates, surface area measurements were made using white light interferometry (WLI), (WYKO NT-2000 Surface Profiler, WYKO Systems) and analyzed via the scanning probe image processor (SPIP<sup>TM</sup> Image Metrology, version 5.1.0).

**2.4. Dissolution Procedure.** The basic CFC design and fabrication procedure was similar to that described previously,<sup>29</sup> but the CFC unit incorporated a mixer section in the outlet to ensure a well-mixed solution for analysis. Figure 2 shows (a) the CFC unit schematically in cross section with the mixer in the outlet and (b) a photograph of a finished channel unit. The geometric area of the crystal exposed to solution was determined by the internal channel dimensions: the width,  $w$ , was 4 mm and length,  $l$ , was 10 mm. The channel height ( $2h$ ) was determined via WLI to be  $210 \pm 10 \mu\text{m}$ . The channel was assembled by simply applying light pressure on the channel unit, placed on the crystal substrate of interest. Inlet and outlet pipes (PVC, 0.318 cm inner diameter and 0.635 cm outer diameter, St. Gobain Plastics) were connected directly to the cell by push-fitting to a syringe pump using Omni-fit adapters (Bio-Chem Fluidics). The syringe pump was from KD Scientific and was equipped with a 50 mL syringe (BD Plastipak, luer-Lok) with a 22 mm inner diameter. This was used to drive solution into the assembled cell. Dissolution experiments took place at flow rates ( $V_f$ ) in the range of  $0.008\text{--}0.167 \text{ cm}^3 \text{ s}^{-1}$ . This corresponds to a maximum contact time of  $\sim 1$  s for solution within the part of the channel above the crystal at the lowest flow rate. Thus, it was possible to change the flow rate and make measurements very easily over a wide range. All CFC measurements were made at  $22 \pm 1^\circ\text{C}$ .

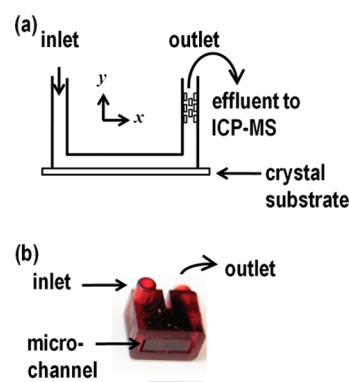


**Figure 2.** Illustration of (a) the two-dimensional cross section of the flow cell (not to scale), highlighting the crystal substrate that forms the base of the channel and the mixer in the outlet. (b) A photograph of a finished CFC unit where the scale bar is 10 mm.

Aliquots ( $5 \text{ cm}^3$ ) of the effluent were collected at intervals for the range of flow rates used. Trace element analysis of dissolved  $\text{Ca}^{2+}$  was carried out on the aliquots via ICP-MS (7500 Agilent), in order to determine the flow rate-dependent outlet concentrations. A Ca standard ( $1 \text{ g/dm}^3$  Fluka, analytical grade) was used to prepare solutions for the calibration curves needed for the quantification of  $\text{Ca}^{2+}$  in each aliquot.

### 3. MASS TRANSPORT AND KINETIC MODELING

Numerical simulations were performed on a Dell Intel core 2 Quad 2.49 GHz computer equipped with 8GB of RAM and running Windows XP Professional X64 bit 2003 edition. Modeling was performed using the commercial finite element modeling package Comsol Multiphysics 3.5a (Comsol AB, Sweden), using the Matlab interface (Release 2009b) (MathWorks Inc., Cambridge, U.K.). Simulations were carried out with  $>51\,000$  triangular mesh elements. Mesh resolution was defined to be finest around the bottom plane of the channel, that is, in the vicinity of the surface of the crystal substrate where the concentration gradient was steepest. Simulations with finer meshes were carried out (not reported) to confirm that the mesh was sufficiently fine to ensure that the predicted solutions were accurate (better than 0.01% variance).

**3.1. Theory.** The channel was simulated as a 2D cross section along the channel length ( $l$ ), as illustrated in Figure 3a. Because  $w \gg h$ , edge effects in the  $w$  direction were neglected, to render a 3D model unnecessary.

**3.1.1. Hydrodynamics.** The incompressible Navier–Stokes equations for momentum balance (eq 1) and continuity (eq 2) were solved under steady-state conditions for the cross-sectional domain shown in Figure 3a

$$\rho \mathbf{V} \cdot \nabla \mathbf{V} = -\nabla p + \eta \nabla^2 \mathbf{V} \quad (1)$$

$$\nabla \cdot \mathbf{V} = 0 \quad (2)$$

where  $\rho$  is the density of the solution ( $1.00 \text{ g cm}^{-3}$  was used, as for water),  $\mathbf{V}$  is the velocity vector (with components  $u$  and  $v$  in the  $x$  and  $y$  directions, respectively),  $p$  is the pressure,  $\eta$  is the dynamic viscosity assumed to be  $1.00 \text{ mPa s}$ ,  $\nabla$  is the vector differential operator, and  $\nabla^2$  is the vector laplacian operator.

The hydrodynamic behavior within the channel cell, as described by the incompressible Navier–Stokes equations, was



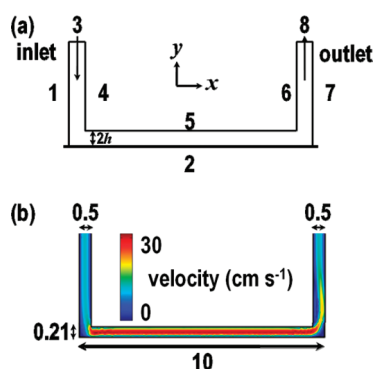


**Figure 3.** 2D representations of (a) the channel geometry used for finite element modeling simulations where the numbers represent the boundaries (edges) used in simulations (not to scale) and (b) the velocity profile of solution within the flow cell for the case of  $V_f = 0.1649 \text{ cm}^3 \text{ s}^{-1}$ . The cell dimensions in (b) are in millimeters and were used throughout.

solved for the following boundary conditions, where the boundaries are defined in Figure 3a

$$\text{boundaries 1, 2, and 4–7: } u = 0, v = 0 \quad (3)$$

$$\text{boundary 3: } u = 0, v = -\frac{V_f}{wx_{\text{ch}}} \quad (4)$$

$$\text{boundary 8: } \mathbf{n} \cdot \eta \nabla^2 \mathbf{V} = 0 \quad (5)$$

where  $x_{\text{ch}}$  is the channel height at the inlet (length of boundary 3, 0.5 mm) and  $\mathbf{n}$  is the inward pointing vector normal to a particular boundary. The condition on boundary 3 (eq 4) is plug flow into the cell.

**3.1.2. Convective–Diffusive Mass Transport.** Once the velocity components  $u$  and  $v$  within the CFC had been determined, the local velocity vectors were used in the solution of the convective–diffusion equations, to predict the concentration distribution in the cell and, especially, in the region of the outlet. The convective–diffusion equation was solved under steady-state conditions

$$D_i \nabla^2 c_i - \mathbf{V} \cdot \nabla c_i = 0 \quad (6)$$

where  $D_i$  is the diffusion coefficient of the species of interest,  $i$ , and  $c_i$  is the concentration of species  $i$ . Because the two dissolving species have similar diffusion coefficients ( $0.792 \times 10^{-5}$  and  $1.065 \times 10^{-5} \text{ cm}^2 \text{ s}^{-1}$  for  $\text{Ca}^{2+}$  and  $\text{SO}_4^{2-}$ , respectively, at infinite dilution), the mean diffusion coefficient was used for the purposes of simulations, thereby facilitating the solution for one species only. This is appropriate given that the studies were for stoichiometric dissolution into a medium comprising little or no additional electrolyte. The following boundary conditions applied to the flow cell

$$\text{boundaries 1, 4–7: } \mathbf{n} \cdot \mathbf{N} = 0 \quad (7)$$

$$\text{boundary 2: } \mathbf{n} \cdot \mathbf{N} = k_{\text{diss}}(c_{\text{eq}} - c_i) \quad (8)$$

$$\text{boundary 3: } c_i = 0 \quad (9)$$

$$\text{boundary 8: } \mathbf{n} \cdot (-D_i \nabla c_i) = 0 \quad (10)$$

where  $\mathbf{N}$  is the vector flux of the species,  $k_{\text{diss}}$  is a heterogeneous rate constant, and  $c_{\text{eq}}$  is the equilibrium concentration for the

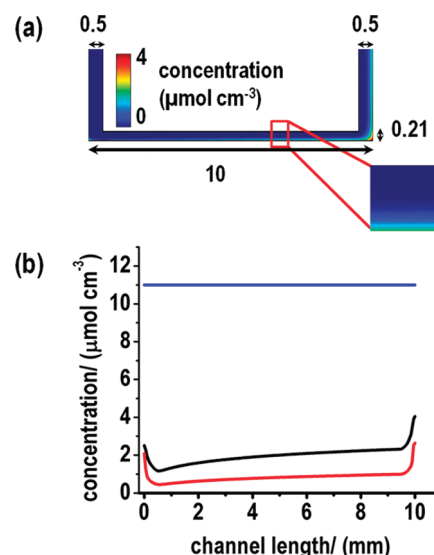


**Figure 4.** Illustration of (a) the CFC cross section depicting the concentration for  $V_f = 0.0083 \text{ cm}^3 \text{ s}^{-1}$  and  $k_{\text{diss}} = 1 \times 10^{-3} \text{ cm s}^{-1}$  where dimensions are in millimeters. (b) The corresponding interfacial concentration along the length of the channel for  $V_f = 0.0083 \text{ cm}^3 \text{ s}^{-1}$  (black) and  $V_f = 0.1649 \text{ cm}^3 \text{ s}^{-1}$  (red), with an applied rate constant  $k_{\text{diss}} = 1 \times 10^{-3} \text{ cm s}^{-1}$  in each case. For comparison, the saturated solution concentration is shown (blue).

solid/saturated solution, when bulk ionic strength effects due to any added dissolved salts are taken into account. Herein, we used  $c_{\text{eq}} = 11 \text{ mM}$  (gypsum) and  $16 \text{ mM}$  (calcium sulfate anhydrite) as calculated by MINEQL<sup>+</sup>; the gypsum value is close to that deduced from experiments.<sup>15</sup> For gypsum experiments with  $0.03 \text{ M}$  added electrolyte,  $c_{\text{eq}} = 14 \text{ mM}$  was used. Mass transport across boundary 8 is due to convection only. Because the dissolution fluxes for most of the systems of interest were relatively low, we did not model any spatial variations in ionic strength as these effects would be relatively minor. For simplicity, we chose a first-order rate law (eq 8): this has been used previously for gypsum and related materials<sup>12a,18c,35</sup> and, further, was reasonable because the reaction was generally very far from equilibrium under the conditions of the experiments.

## 4. RESULTS AND DISCUSSION

**4.1. Insights from Simulations.** The finite element simulations provide information on the processes occurring in the cell. In particular, the approach described yields: (i) the hydrodynamic behavior within the CFC chamber, from which velocity profiles, in regions of interest, can be extracted; (ii) concentration profiles of dissolved species within the cell, which informs on the kinetic/mass transport regime; and (iii) the flow rate-dependent outlet concentration, which is the variable used to analyze experimental data. We use the simulations to highlight briefly some of the main features of the techniques for the case of gypsum ( $c_{\text{eq}} = 11 \text{ mM}$ ). Figure 3b shows a typical example of the velocity profile of solution in the flow cell ( $2h = 0.21 \text{ mm}$ ) at  $V_f = 0.1649 \text{ cm}^3 \text{ s}^{-1}$ . A steady laminar Poiseuille profile is established and maintained along the channel length, after a short lead-in length.

Figure 4 shows (a) a typical concentration profile in the CFC for  $V_f = 0.0083 \text{ cm}^3 \text{ s}^{-1}$  and  $k_{\text{diss}} = 1 \times 10^{-3} \text{ cm s}^{-1}$  and (b) plots of the concentration of the dissolved species at the crystal/solution interface along the length of the channel for

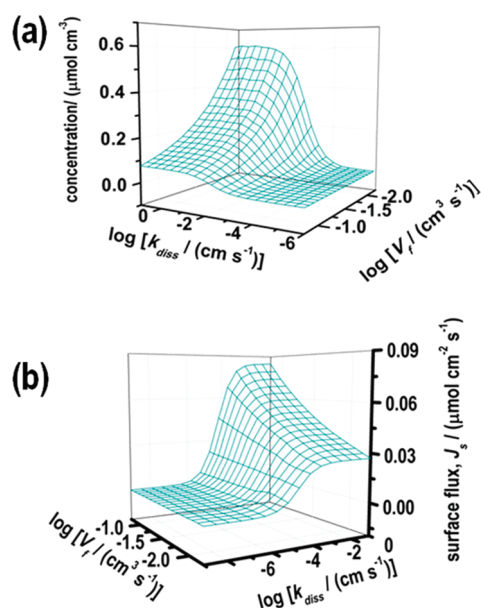


**Figure 5.** (a) Simulated outlet concentrations and (b) mean surface flux,  $J_s$ , as a function of  $k_{\text{diss}}$  and  $V_f$ . The channel cell was characterized by the parameters shown in Figure 3b.

$V_f = 0.0083 \text{ cm}^3 \text{ s}^{-1}$  and  $0.1649 \text{ cm}^3 \text{ s}^{-1}$ , which correspond to the lower and higher  $V_f$  limits of those used herein. The  $k_{\text{diss}}$  value is typical of that found in the experimental studies (vide infra). A consequence of the high mass transport rates that can be generated in the channel is that the concentration boundary layer above the dissolving substrate is relatively thin, allowing fast surface kinetics to be investigated. This is evident from Figure 4b, which shows that the interfacial concentration is considerably lower than the equilibrium value at the extreme limits of typical flow rates, indicating substantial surface kinetic control of the reaction for these parameters. The nonuniform concentration profiles along the channel length are a consequence of the nonuniform accessibility of the channel system<sup>36</sup> between 0.5 and 9.5 mm, coupled with stagnation zones that develop at the chamber edges. This leads to higher interfacial concentration values between 0 and 0.5 mm (upstream portion of the crystal) and 9.5 and 10 mm (downstream portion). However, these stagnation zones make a very minor contribution to the total surface flux from the entire exposed crystal.

Figure 5 shows 3D plots of the outlet concentration (a) and average surface flux (b) as a function of the kinetic constant,  $k_{\text{diss}}$ , and flow rate,  $V_f$ . For any particular flow rate, an increase in  $k_{\text{diss}}$  results in an increase in the surface flux and outlet concentration, as a consequence of increasing generation of dissolution products from the crystal surface up to a maximum ( $k_{\text{diss}}$ -independent value) where the reaction becomes transport-controlled. In addition, it can be seen that, for any rate constant, the highest outlet concentration is predicted at low flow rates, essentially because the duration of interaction between the crystal surface and solution in the cell is then longer, thereby allowing dissolution products to accumulate more readily in the solution. In the regime  $k_{\text{diss}} > 0.1 \text{ cm s}^{-1}$ , for the range of  $V_f$  shown, the reaction becomes transport-limited. Below this value, surface kinetic determination is possible.

**4.2. Dissolution Kinetics.** **4.2.1. Surface Analysis.** WLI measurements were made to determine the surface topography of the

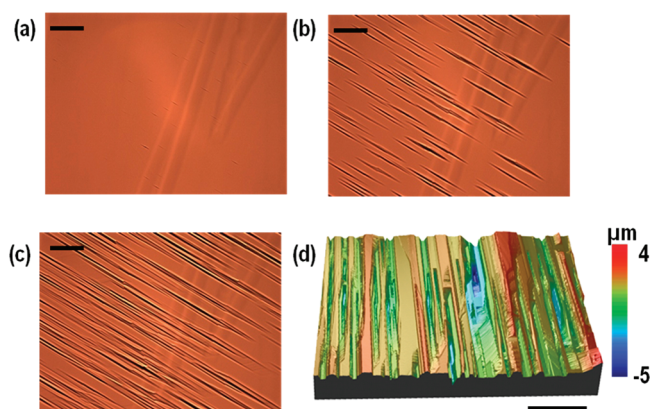


**Figure 6.** Typical DIC micrographs (scale bars, 100  $\mu\text{m}$ ) of the (010) cleaved gypsum surface after etching in pure  $\text{H}_2\text{O}$  for (a) 90 s, (b) 10 min, and (c) 30 min and (d) the corresponding WLI micrograph after a 30 min etch, where the scale bar is 30  $\mu\text{m}$ .

crystal surfaces before and after CFC studies, with the aim of determining the specific surface area of the crystal surface exposed to the solution. This was primarily to confirm that the surface area was constant over the duration of a CFC experiment and to determine the roughness factor ( $\lambda$ ) with which flux values predicted by simulations could be normalized to allow comparison between different materials and to obtain intrinsic dissolution rates.

Figure 6 depicts typical differential interference contrast (DIC) micrographs of the basal plane gypsum surface after etching in ultrapure  $\text{H}_2\text{O}$  for (a) 90 s, (b) 10 min, and (c) 30 min and (d) a WLI micrograph after a 30 min etch. The micrographs clearly show an alteration in surface topography, from early times in the dissolution process (Figure 6a), where small etch features are isolated on the (010) cleavage surface. With time, these features grow and achieve complete coalescence by  $\sim 30$  min (Figure 6c), and the surface topology and roughness ( $\lambda$ ) essentially remain similar for times thereafter.  $\lambda$  was found to be in the range of 1.1–1.2, 1.9–3.3, and 1.6–4.4 for (010) gypsum, edge plane gypsum, and anhydrite, respectively. The highest  $\lambda$  value (roughest sample used for experiments) yielded an rms roughness value of 4.5  $\mu\text{m}$  constituting 2.3% of the channel height ( $2h$ ), which was considered unlikely to disrupt the cell hydrodynamics described above, as evidenced by the fact that electrodes deployed in channel cells are only slightly smoother than this and conform well to predictions for a smooth surface.<sup>24–26,29</sup> In addition,  $\lambda$  values for each sample were within  $\pm 10\%$  when examined before and after CFC studies.

**4.2.2. CFC Dissolution Measurements.** As mentioned above, the dissolution reaction was monitored via flow rate-dependent off-line ICP-MS analysis on CFC effluent for  $\text{Ca}^{2+}$  at each flow rate. At least four replicate runs were made for each flow rate. These data were then analyzed, using the model described, to obtain values for the heterogeneous rate constant ( $k_{\text{diss}}$ ) for the dissolution of each substrate.

Figure 7 shows typical experimental data, of outlet  $\text{Ca}^{2+}$  concentration as a function of flow rate for the three different crystal substrates. The error bars in this plot and that in Figure 8 reflect two standard deviations calculated from four replicate runs from ICP-MS data at each flow rate shown. The solid lines represent the best fit of  $k_{\text{diss}}$  for each substrate, as predicted from simulations. The etched surface of basal plane gypsum exhibited

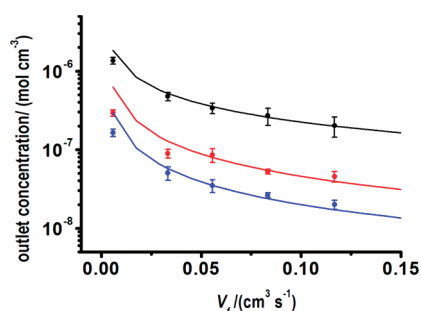


**Figure 7.** Cell outlet concentration as a function of flow rate for the dissolution of etched basal plane gypsum (red), edge plane gypsum (black), and anhydrite (blue). The solid line corresponds to the best fits to the model with a rate constant,  $k_{\text{diss}}$  ( $\text{cm s}^{-1}$ ), of  $6.0 (\pm 1.5) \times 10^{-4}$ ,  $> 0.1$ , and  $7.8 (\pm 1.3) \times 10^{-4} \text{ cm s}^{-1}$ , for basal plane gypsum, edge plane gypsum ( $c_{\text{eq}} = 11 \text{ mM}$  for gypsum), and anhydrite ( $c_{\text{eq}} = 16 \text{ mM}$ ), respectively. The simulation used other parameters stated in the text.

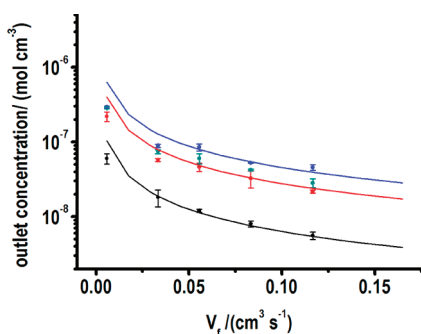


**Figure 8.** Outlet concentration as a function of flow rate for dissolution of the etched basal plane of gypsum in 5 mM solutions of *l*-tartaric acid (blue points), *d*-tartaric acid (green points), and STMP (black) and in pure  $\text{H}_2\text{O}$  (red). The solid lines correspond to the best fit rate constant,  $k_{\text{diss}}$  ( $\text{cm s}^{-1}$ ), predicted by simulations with values of  $6.0 (\pm 1.5) \times 10^{-4}$  and  $1.3 (\pm 0.5) \times 10^{-4} \text{ cm s}^{-1}$  for pure  $\text{H}_2\text{O}$  and STMP, respectively, whereas *l*-tartaric and *d*-tartaric acids exhibit a similar rate constant of  $7.3 (\pm 2.0) \times 10^{-4} \text{ cm s}^{-1}$  (blue solid line).

the lowest value of  $k_{\text{diss}} = 6.0 (\pm 1.5) \times 10^{-4} \text{ cm s}^{-1}$ , whereas that of anhydrite was slightly higher at  $k_{\text{diss}} = 7.8 (\pm 1.3) \times 10^{-4} \text{ cm s}^{-1}$ . The excellent agreement between experiments and predictions from simulations observed here, particularly in the high flow rate range, justifies the choice of a first-order rate law for basal plane gypsum and anhydrite dissolution in pure  $\text{H}_2\text{O}$ . At lower flow rates, the model tends to overestimate the outlet concentrations. Under these conditions, the interfacial concentrations move closer to equilibrium and the small deviation between theory and experiment may indicate a change in the reaction order. Notably, edge plane gypsum yielded a rate constant of  $k_{\text{diss}} > 0.1 \text{ cm s}^{-1}$ , indicating a mass-transport-controlled dissolution process under the experimental conditions.

With these rate constants, the associated intrinsic dissolution fluxes  $J_0$  ( $\text{mol cm}^{-2} \text{ s}^{-1}$ ) =  $k_{\text{diss}} \times c_{\text{eq}}$ , taking into account  $\lambda$  in the calculation of the area, were deduced to be  $5.7 (\pm 1.4) \times 10^{-9}$  and  $4.0 (\pm 0.7) \times 10^{-9} \text{ mol cm}^{-2} \text{ s}^{-1}$  for basal plane gypsum (010) and anhydrite, respectively. The kinetics found for gypsum compare favorably with the values deduced by Colombani<sup>14</sup> of  $J_0 = 5 (\pm 2) \times 10^{-9} \text{ mol cm}^{-2} \text{ s}^{-1}$ . The intrinsic dissolution flux for anhydrite crystal compares well with recent values from Jeschke and Dreybrodt, who obtained  $J_0 = 5 (\pm 1) \times 10^{-9} \text{ mol cm}^{-2} \text{ s}^{-1}$ .<sup>16</sup>

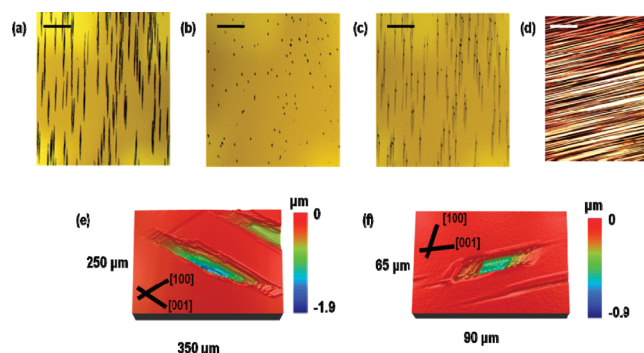


**Figure 9.** DIC micrographs of the (010) surface of gypsum (matched halves) after a 20 min of etching in (a)  $\text{H}_2\text{O}$  and (b) 5 mM STMP. The two surfaces (a and b) are superimposed in (c) to show correspondence of etch pits on the surfaces. A cleaved gypsum surface etched for 20 min in 0.03 M  $\text{KNO}_3$  is shown in (d) for comparison. The scale bars are 300  $\mu\text{m}$ . WLI micrographs of pit morphology after etching for 20 min in (e)  $\text{H}_2\text{O}$  and (f) 5 mM STMP are also shown. The main crystallographic directions with respect to the etch pits formed on the (010) surface are indicated and the [010] direction normal to the surface.

However, these values are much smaller than the value of  $J_0 = 2 \pm 1 \times 10^{-8} \text{ mol cm}^{-2} \text{ s}^{-1}$  deduced from anhydrite polycrystalline pellets.<sup>12b</sup> It is important to point out that we have analyzed natural polycrystalline anhydrite samples that have been deposited over geological time scales such that the crystalline deposits are compacted to an extent that porosity is negligible. In contrast, anhydrite pellets, such as those used in some previous studies,<sup>12b</sup> are typically formed by dehydrating gypsum pellets, a process that exposes the sample to thermal shock, possibly further weakening the sample structure. This typically results in samples with high specific surface areas that would naturally produce higher dissolution fluxes defined in terms of the geometric area of the sample.

It is further important to note that, with the CFC method, we eliminate the possibility of surface concentrations (from generation of dissolution products) approaching the gypsum saturation point, by probing anhydrite dissolution under far from equilibrium conditions via the high rates of mass transport that can be generated.

**4.2.3. Effect of Additives.** We next consider the influence of key additives on gypsum dissolution. Figure 8 shows plots of outlet concentration as a function of flow rate for etched basal plane gypsum in the presence of STMP, *l*-tartaric acid, and *d*-tartaric acid, with  $\text{H}_2\text{O}$  also shown. These additives were chosen because of their extensive use as inhibitors of humid creep, in the production of  $\text{CaSO}_4$ -based materials.<sup>20,21</sup> In each case, there is good agreement between the experimental data and the first-order model proposed (which takes into account the ionic strengths of the different solutions in calculating  $c_{\text{eq}}$ ; see Table 1). Rate constants for dissolution in the presence of *d*-tartaric and *l*-tartaric acids were found to be similar (within experimental error) and close to that for pure  $\text{H}_2\text{O}$ , with  $k_{\text{diss}} = 7.3 (\pm 2.0) \times 10^{-4} \text{ cm s}^{-1}$ , which shows that *d*- and *l*-tartaric acids have relatively little effect on gypsum dissolution under the experimental conditions. However, in the presence of STMP, the rate constant was much lower,  $k_{\text{diss}} = 1.3 (\pm 0.5) \times 10^{-4} \text{ cm s}^{-1}$ , indicating a significant retardation of the dissolution process.

To elucidate and explain the mode of action of STMP on the process of gypsum dissolution, we carried out etch pit studies for



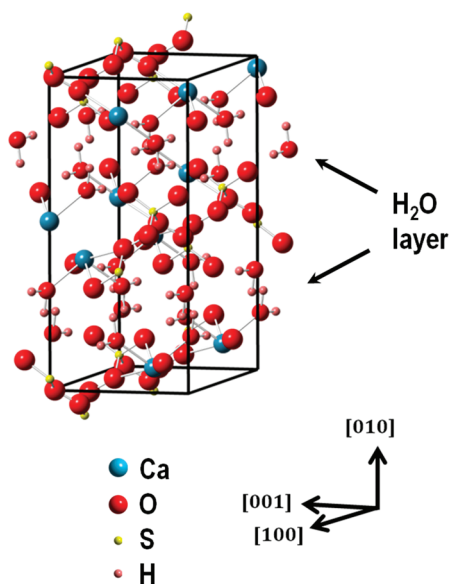


**Figure 10.** Gypsum unit cell with the main crystallographic directions indicated. Note the H<sub>2</sub>O layer interspaced between CaSO<sub>4</sub> bilayers.

dissolution in quiescent solution for a period of 20 min. By careful cleaving along the (010) gypsum plane, mirror surfaces were produced. One half was etched in STMP, whereas the other was etched in ultrapure H<sub>2</sub>O. There is almost complete dissociation of STMP, yielding a solution ionic strength of ca. 0.03 M. To investigate ionic strength effects, etching was also carried out in 0.03 M KNO<sub>3</sub>.

Figure 9 shows DIC micrographs of the resulting etch pits, where (a) is the surface after etching in H<sub>2</sub>O, (b) the mirror surface when etched in STMP, (c) the superimposition of (a) and (b), and (d) a gypsum surface after etching in KNO<sub>3</sub>. When the two microstructures in (a) and (b) are superimposed (c), it is clear that there is an exact correspondence between the positions of etch pits, and therefore, both pit types emerge from the same defect sites that presumably run through the crystal. Notably, however, there is a drastic difference in the pit sizes, with STMP retarding dissolution compared to water. This effect is even more striking when one considers that the higher ionic strength of the STMP solution would be expected to promote dissolution if it simply acted as an inert salt, as evidenced by the KNO<sub>3</sub> data (Figure 9d).

Figure 9 also shows isolated pits that result from etching in water (e) and STMP (f). In the case of H<sub>2</sub>O, the pits are irregular hexagons with two parallel edges aligned along the [001] and [100] directions and one poorly defined edge (Figure 9e); see Figure 10 for the gypsum unit cell. The pits were found to exhibit typical dimensions of  $350 \pm 30$ ,  $62 \pm 14$ , and  $1.9 \pm 0.5 \mu\text{m}$  in the [001], [100], and [010] directions, respectively, after etching for 20 min. In contrast, etching in the presence of STMP produced pits with the shape of a parallelogram, laterally embracing the [001] and [100] directions only (Figure 9f). The etch pits were also relatively small compared with those produced when etching in pure water, with typical dimensions of  $90 \pm 10$ ,  $36 \pm 6$ , and  $1.4 \pm 0.5 \mu\text{m}$  in the [001], [100], and [010] directions, respectively. The elongated etch pit morphologies indicate preferential dissolution in the [001] direction relative to the [100] etching in pure H<sub>2</sub>O. Indeed, much faster dissolution along the [001] direction relative to the [100] direction may be responsible

for the development of the irregular pit edge (Figure 9e). In the presence of STMP, dissolution in the [001] and [100] directions was retarded to different extents so that the rates became closer in magnitude, resulting in the parallelogram pit shape observed. Because STMP dissociates to  $\text{P}_3\text{O}_9^{3-}$ ,<sup>37</sup> under the experimental conditions, it is likely that STMP will have a binding affinity with surface calcium ion sites, inhibiting dissolution. The anion has a chair configuration with the phosphate groups facing outward from the ring (Figure 1), giving it the capacity to adsorb onto several positively charged sites on the crystal surface and form surface complexes.<sup>38,39</sup>

For both etchants (H<sub>2</sub>O and STMP), dissolution in the [010] direction (etch pit depth) was much slower than in the other directions analyzed. However, the values obtained with and without STMP were similar, indicating little effect of STMP on dissolution in this direction. Dissolution in the [010] direction involves periodic removal of the water layer interspaced between CaSO<sub>4</sub> bilayers in the gypsum crystal. The fact that STMP has little influence suggests that detachment of the water layer may be rate-limiting in this direction.

## 5. CONCLUSIONS

The dissolution kinetics of gypsum and calcium sulphate anhydrite have been obtained and analyzed via the CFC method, coupled with off-line ICP-MS for the measurement of dissolved Ca<sup>2+</sup> from the crystal surface. For the first time, it has been possible to distinguish between the dissolution kinetics for the basal (010) and edge plane (001) surfaces of gypsum: radically different dissolution characteristics have been observed. The basal surface exhibited an intrinsic flux,  $J_0 = 5.7 (\pm 1.4) \times 10^{-9} \text{ mol cm}^{-2} \text{ s}^{-1}$  into pure water ( $k_{\text{diss}} = 6.0 (\pm 1.5) \times 10^{-4} \text{ cm s}^{-1}$ ), whereas the edge plane exhibited high rate constant values,  $k_{\text{diss}} > 0.1 \text{ cm s}^{-1}$ , indicating a transport-controlled process under the experimental conditions applied. Anhydrite crystals exhibited fluxes of  $J_0 = 4.0 (\pm 0.7) \times 10^{-9} \text{ mol cm}^{-2} \text{ s}^{-1}$  into pure water ( $k_{\text{diss}} = 7.8 (\pm 1.3) \times 10^{-4} \text{ cm s}^{-1}$ ).

The effect of additives on dissolution of the basal gypsum surface considered molecules that have been used industrially as inhibitors of humid creep in CaSO<sub>4</sub>-based building materials. It was observed that tartaric acid (*d*- and *l*-) had little influence on dissolution kinetics with rates similar to those observed when dissolution was carried out in pure water. In the presence of STMP, dissolution rates were much lower,  $J_0 = 1.6 (\pm 0.6) \times 10^{-9} \text{ mol cm}^{-2} \text{ s}^{-1}$  ( $k_{\text{diss}} = 1.3 (\pm 0.5) \times 10^{-4} \text{ cm s}^{-1}$ ), despite the high ionic strength associated with the additive, which would be expected to promote dissolution (salting-in). Etching studies revealed that STMP significantly inhibits gypsum dissolution across the basal surface but has a lower inhibitory effect in the [010] direction (normal to the basal surface). The mode of action is likely to involve surface complexation of SMTP anions on the crystal surface. The lack of any significant effect in the [010] tentatively suggests that the loss of the water layer may be the rate-limiting process in this direction for which STMP would have little influence.

The studies herein illustrate how the CFC method is particularly powerful in elucidating surface kinetics and the role of mass transport in the interfacial processes. The methodology is flexible and allows the study of particular crystal faces and the introduction of inhibitors. When coupled with simple etching methods, one can obtain a good level of information on kinetics, mechanisms, and the mode of action of inhibitors on dissolution.



## AUTHOR INFORMATION

## Corresponding Author

\*E-mail: p.r.unwin@warwick.ac.uk

## ACKNOWLEDGMENT

This work was supported by Saint-Gobain Gyproc (funding for M.M.M.) and the European Research Council (funding for P.R.U., M.P., and M.E.S.), to whom we are grateful. We thank Maxim Joseph for assistance with microstereo lithography of the flow cells and P. Aston and Dr. L. Jong for assistance with ICP-MS. We also thank I. Wilkes and H. Jaffel at St. Gobain Gyproc for helpful discussions. The light microscopy and ICP-MS equipment used in this research was obtained through Birmingham Science City with support from Advantage West Midlands and the European Regional Development Fund.

## REFERENCES

- (1) Ford, D. C.; William, P. W. *Karst Geomorphology and Hydrology*; John Wiley & Sons: West Sussex, U.K., 2007.
- (2) Klimchouk, A.; Andrejchuk, V., Eds. *Int. J. Speleol.* **1996**, *25*, 9.
- (3) Bosbach, D.; Junta-Rosso, J. L.; Becker, U.; Hochella, M. F., Jr. *Geochim. Cosmochim. Acta* **1996**, *60*, 3295.
- (4) James, A. N. *Soluble Materials in Civil Engineering*; Ellis Horwood: Chichester, U.K., 1992.
- (5) Van Rosmalen, G. M.; Daudey, P. J.; Marchee, G. J. *J. Cryst. Growth* **1981**, *52*, 801.
- (6) Livingston, R.; Wolde-Tinsae, A.; Chaturbahai, A. In *Structural Repair and Maintenance of Historical Buildings*; Brebbia, C. A., Ed.; Computational Mechanics Publications: Southampton, U.K., 1991; Vol. 1, p 157.
- (7) Charola, A. E.; Puhlinger, J.; Steiger, M. *Environ. Geol.* **2007**, *52*, 339.
- (8) Cowan, J. C.; Weintritt, D. J. *Water-Formed Scale Deposits*; Gulf Publishing Company: Houston, TX, 1976.
- (9) Vetter, O. J. G.; Philips, R. C. *J. Pet. Technol.* **1970**, *22*, 1299.
- (10) See, for example: (a) Lasaga, A. C.; Blum, A. E. *Geochim. Cosmochim. Acta* **1986**, *50*, 2363. (b) Schott, J.; Pokrovsky, O. S.; Oelkers, E. H. *Rev. Mineral. Geochem.* **2009**, *70*, 207.
- (11) See, for example: (a) Lasaga, A. C.; Lüttge, A. *Science* **2001**, *291*, 2400. (b) Lasaga, A. C.; Lüttge, A. *Eur. J. Mineral.* **2003**, *15*, 603. (c) Lüttge, A. *J. Electron. Spectrosc. Relat. Phenom.* **2006**, *150*, 248.
- (12) See, for example: (a) Liu, S.-T.; Nancollas, G. H. *J. Inorg. Nucl. Chem.* **1971**, *33*, 2311. (b) Barton, A. F. M.; Wilde, N. M. *Trans. Faraday Soc.* **1971**, *67*, 3590. (c) Singh, H.; Bajwa, M. S. *Aust. J. Soil Res.* **1990**, *28*, 947. (d) Svensson, U.; Dreybrodt, W. *Chem. Geol.* **1992**, *100*, 129.
- (13) See, for example: (a) Bosbach, D.; Rammensee, W. *Geochim. Cosmochim. Acta* **1994**, *58*, 843. (b) Bosbach, D.; Jordan, G.; Rammensee, W. *Eur. J. Mineral.* **1995**, *7*, 267. (c) Teng, T. H.; Fan, C. *Chem. Geol.* **2007**, *245*, 242.
- (14) Colombani, J. *Geochim. Cosmochim. Acta* **2008**, *72*, 5634 and references therein.
- (15) CRC *Handbook of Chemistry and Physics*, 89th ed.; David, R. L., Ed.; Taylor & Francis: Boca Raton, FL, 2008–2009.
- (16) Jeschke, A. A.; Dreybrodt, W. *Chem. Geol.* **2002**, *192*, 183.
- (17) See, for example: (a) Coquard, P.; Boistelle, R. *Int. J. Rock Mech. Min. Sci. Geomech. Abstr.* **1994**, *31*, 517. (b) Gartner, E. M. *Cem. Concr. Res.* **2009**, *39*, 289.
- (18) See, for example: (a) Orme, C. A.; Noy, A.; Wierzbicki, A.; McBride, M. T.; Grantham, M.; Teng, H. H.; Dove, P. M.; DeYoreo, J. J. *Nature* **2001**, *411*, 775. (b) Morse, J. W.; Arvidson, R. S. *Earth-Sci. Rev.* **2002**, *58*, 51. (c) Arvidson, R. S.; Collier, M.; Davis, K. J.; Vinson, M. D.; Amonette, J. E.; Lüttge, A. *Geochim. Cosmochim. Acta* **2006**, *70*, 583. (d) Vavouraki, A. I.; Putnis, C. V.; Putnis, A.; Koutsoukos, P. G. *Chem. Geol.* **2008**, *253*, 243. (e) Agudo, E. R.; Kowacs, M.; Putnis, C. V.; Putnis, A. *Geochim. Cosmochim. Acta* **2010**, *74*, 1258.
- (19) (a) Freij, S. J.; Godelitsas, A.; Putnis, A. *J. Cryst. Growth* **2005**, *273*, 535. (b) Gledhill, D. K.; Morse, J. W. *Geochim. Cosmochim. Acta* **2006**, *70*, 5802. (c) Harstad, A. O.; Stipp, S. L. S. *Geochim. Cosmochim. Acta* **2007**, *71*, 56. (d) Xu, M.; Higgins, S. R. *Geochim. Cosmochim. Acta* **2011**, *75*, 719.
- (20) Arese, R.; Martin, D.; Rigaudon, M. U.S. Patent Application 20060048680, March 09, 2006.
- (21) Yu, Q.; Sucech, S.; Groza, B.; Mlinac, R.; Jones, F.; Boehnert, F. U.S. Patent 6-632-550, October 14, 2003.
- (22) Macpherson, J. V.; Unwin, P. R. *Chem. Soc. Rev.* **1995**, *24*, 109.
- (23) Unwin, P. R.; Macpherson, J. V. *J. Chem. Soc., Faraday Trans.* **1993**, *89*, 1883.
- (24) See, for example: (a) Compton, R. G.; Pritchard, K. L.; Unwin, P. R.; Grigg, G.; Silvester, P.; Lees, M.; House, W. A. *J. Chem. Soc., Faraday Trans. 1* **1989**, *85*, 4335. (b) Compton, R. G.; Pritchard, K. L.; Unwin, P. R. *J. Chem. Soc., Chem. Commun.* **1989**, 249. (c) Compton, R. G.; Unwin, P. R. *Philos. Trans. R. Soc. London* **1990**, A330, 1. (d) Compton, R. G.; Walker, C. T.; Unwin, P. R.; House, W. A. *J. Chem. Soc., Faraday Trans.* **1990**, *86*, 849. (e) Unwin, P. R.; Compton, R. G. *J. Chem. Soc., Faraday Trans.* **1990**, *86*, 151. (f) Barwise, A. J.; Compton, R. G.; Unwin, P. R. *J. Chem. Soc., Faraday Trans.* **1990**, *86*, 137. (g) Wilkins, S. J.; Compton, R. G.; Taylor, M. A.; Viles, H. A. *J. Colloid Interface Sci.* **2001**, *236*, 354. (h) Thompson, M.; Wilkins, S. J.; Compton, R. G.; Viles, H. A. *J. Colloid Interface Sci.* **2003**, *259*, 338.
- (25) See, for example: (a) Orton, R.; Unwin, P. R. *J. Chem. Soc., Faraday Trans.* **1993**, *89*, 3947. (b) Brown, C. A.; Compton, R. G.; Narramore, C. A. *J. Colloid Interface Sci.* **1993**, *160*, 372. (c) Hong, Q.; Suarez, M. S.; Coles, B. A.; Compton, R. G. *J. Phys. Chem. B* **1997**, *101*, 5557. (d) Booth, J.; Sanders, G. H. W.; Compton, R. G.; Atherton, J. H.; Brennan, C. M. *J. Electroanal. Chem.* **1997**, *440*, 83. (e) Peltonen, L.; Liljeroth, P.; Heikkilä, T.; Kontturi, K.; Hirvonen, Eur. *J. Pharm. Sci.* **2003**, *19*, 395.
- (26) Unwin, P. R.; Compton, R. G. *Comprehensive Chemical Kinetics*; Elsevier: New York, 1989; Vol. 29, Chapter 6, p 173.
- (27) Cooper, J. A.; Compton, R. G. *Electroanalysis* **1997**, *10*, 141.
- (28) Compton, R. G.; Pritchard, K. L. *Philos. Trans. R. Soc. London* **1990**, A330, 47.
- (29) Snowden, M. E.; King, P. H.; Covington, J. A.; Macpherson, J. V.; Unwin, P. R. *Anal. Chem.* **2010**, *82*, 3124.
- (30) Schecher, W. D.; McAvoy, D. C. *MINEQL+: A Chemical Equilibrium Modelling System*; Environmental Research Software: Hallowell, ME, 2003.
- (31) Davies, C. W. *Ion Association*; Butterworths: London, 1962.
- (32) See, for example: (a) White, A. F.; Brantley, S. L. *Rev. Mineral. Geochem.* **1995**, *31*, 1. (b) Brantley, S. L.; Mellot, N. R. *Am. Mineral.* **2000**, *85*, 1767. (c) Lüttge, A. *Am. Mineral.* **2005**, *90*, 1776.
- (33) Bruckenstein, S. *Anal. Chem.* **1985**, *57*, 371.
- (34) Unwin, P. R.; Compton, R. G. *J. Electroanal. Chem. Interfacial Electrochem.* **1988**, *245*, 287.
- (35) Colombani, J.; Bert, J. *Geochim. Cosmochim. Acta* **2007**, *71*, 1913.
- (36) See, for example: (a) Compton, R. G.; Unwin, P. R. *J. Electroanal. Chem. Interfacial Electrochem.* **1986**, *205*, 1. (b) Compton, R. G.; Pilkington, M. B. G.; Stearn, G. M.; Unwin, P. R. *J. Electroanal. Chem. Interfacial Electrochem.* **1987**, *238*, 43.
- (37) See, for example: (a) Jones, H. W.; Monk, C. B.; Davies, C. W. *J. Chem. Soc.* **1949**, 2693. (b) Jones, H. W.; Monk, C. B. *J. Chem. Soc.* **1950**, 3475.
- (38) Liu, S. T.; Nancollas, G. H. *J. Colloid Interface Sci.* **1975**, *52*, 582.
- (39) Rashichi, F.; Finch, J. A. *Miner. Eng.* **2000**, *13*, 1019.